Inorganic Chemistry
Article
Cite This: *Inorg. Chem.* XXXX, XXX, XXX−XXX
pubs.acs.org/IC

Spontaneous Polarization Effect and Photocatalytic Activity of Layered Compound of $BiOIO_3$

Xu-Dong Dong, Guo-Ying Yao, Qing-Lu Liu, Qing-Meng Zhao, and Zong-Yan Zhao*

Faculty of Materials Science and Engineering, Kunming University of Science and Technology, Kunming 650093, P. R. China

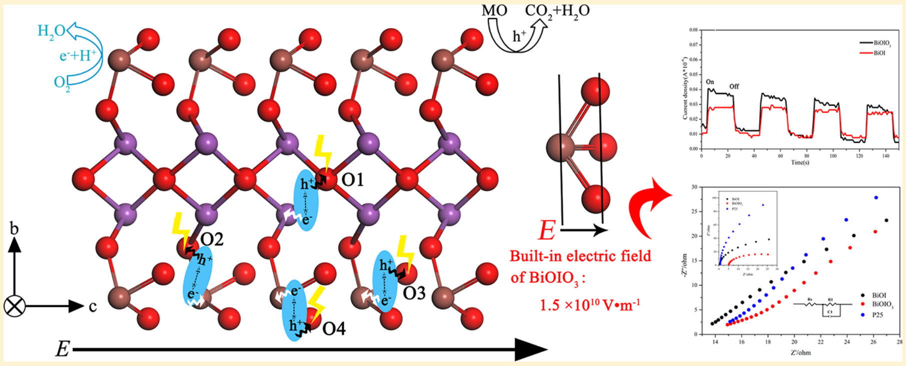

ABSTRACT: Internal polarized electric field is found to be an effective and available strategy to separate photogenerated electron−hole pairs. By this method, the efficiency of photocatalytic reactions can be obviously enhanced. Here, the layered compound of $BiOIO_3$ with spontaneous polarization was synthesized by a simple hydrothermal method. Taking another bismuth compound BiOI as a counterpart, which has a similar layered structure, the spontaneous polarization effects of $BiOIO_3$ were analyzed and confirmed. The photocatalytic activity of $BiOIO_3$ and BiOI were evaluated by the degradation of methyl orange. Methyl orange was almost completely photocatalytically decomposed by $BiOIO_3$ and BiOI in 40 and 90 min, respectively. The separation and transfer behaviors of photogenerated electron−hole pairs were investigated by a series of photoelectrochemical characterizations. It is further proved the separation and transmission efficiency of $BiOIO_3$ are higher than those of BiOI. According to the results of density of theory calculations, the internal polarized electric field in $BiOIO_3$ is ascribed to the spatial asymmetry of the IO_3 group, which is estimated to $\sim 1.5 \times 10^{10}$ V/m. Under the action of this internal polarized electric field, the photogenerated electrons and holes would transfer along opposite directions, i.e., photogenerated electrons and holes respectively gather at the Bi/I side and O side. Additionally, superoxide radicals ($\bullet O_2^-$) and holes (h^+) are produced during the degradation process, which are responsible for the high visible-light photocatalytic activity. Finally, the cyclic degradation test proves that its photocatalytic performance has long-term stability. Therefore, $BiOIO_3$ polar material can be used as one of the alternative materials for efficient photocatalytic reaction.

1. INTRODUCTION

With the increasingly severe situation of energy shortage and environmental deterioration, photocatalytic technology is one of the promising strategies to solve the above two issues due to its ability to produce hydrogen from water splitting and photocatalytic decompose pollutants. However, traditional photocatalysts (for example, TiO_2, WO_3, ZnO, and so on) usually have a wide band gap and low quantum conversion efficiency, which seriously restrict the further development and practical application of photocatalytic technology. According to current research reports, metal/nonmetal doping, dye/narrowband semiconductor sensitization, plasma metal loading, and novel visible/NIR-light-driven photocatalysts have achieved broad spectral response, but their quantum conversion efficiency needs to be further improved.[1] Hence, numerous efforts are concentrated on improving the quantum efficiency of semiconductor photocatalytic materials. In recent years, internal electric fields have become one of the hotspots in the research field of photocatalytic materials as an internal driving force to improve the separation rate of photogenerated electron−hole pairs.[2]

The origin of an internal electric field in photocatalytic materials mainly includes polarization of ferroelectric materials, semiconductor p-n heterojunction, polarized surface, lattice distortion caused by doping, and spontaneous polarization effect of polar materials. In 2004, Grosso et al. first proposed the application potential of ferroelectric materials in photocatalysis.[3] The spontaneous polarization of ferroelectric materials produces a charged surface that drives carriers to migrate in the opposite direction to separate photogenerated electron−hole pairs. In the case of semiconductor p-n heterojunctions, due to the difference in the Fermi energy levels between the p-type and n-type semiconductors, charge transfer occurs between the two and ultimately reaches equilibrium. The redistribution of charge creates an internal

Received: August 2, 2019

DOI: 10.1021/acs.inorgchem.9b02328
Inorg. Chem. XXXX, XXX, XXX−XXX

electric field that points from the n-region space charge region to the p-region space charge region, thereby facilitating the separation of photogenerated carriers.[4] Wang et al.[5] studied the transfer behavior of photogenerated electrons in ZnO/Cu_2O heterojunctions under the action of an electric field and confirmed that the internal electric field between the two interfaces can promote the separation and migration of carriers. In regard to the heterojunction, due to the different crystal structure and electronic structure of the two phases, the positions of the conduction band and valence band are different, and an internal electric field is formed at the interface which can accelerate the separation of carriers. Li et al.[6] reported that the surface heterojunction formed by α-Ga_2O_3 and β-Ga_2O_3 has good photocatalytic properties. The polarity of the material surface depends on the surface atomic composition and crystal structure, and the exposed polar surface of the crystal can form an electric field, which in turn affects the photocatalytic properties of the material. Yang et al.[7] prepared NiO octahedron photocatalytic material with a polar (111) surface and found that its catalytic degradation of dye molecules is much more active than P25. The internal electric field generated by the spontaneous polarization between the polar (111) and (111) crystal faces will accelerate the photogenerated charge separation, allowing the reduction and oxidation reactions to proceed on the two crystal faces, respectively. In addition, the doping and modification of traditional photocatalysts can lead to lattice distortions in their crystal structures and generate an internal electric field. Cai et al.[8] researched the I-doped anatase TiO_2, and calculations showed that the TiO_6 octahedrons adjacent to iodine atoms were so heavily distorted that the center of the gravity deviated from the position of the Ti^{4+} ion, resulting in a dipole moment of 1.39 D. Although the internal electric field generated by these mechanisms can improve quantum efficiency to some extent, there are still some shortcomings. For example, although the interface electric field of the heterojunction can promote the separation of photogenerated carriers, defects are easily formed at the interface, and the interface electric field has a narrower range and less strength. It does not effectively improve the separation efficiency of photogenerated carriers. Similarly, the internal electric field generated by doping and modification causing lattice distortion is beneficial to the separation of photogenerated carriers. However, due to the introduction of impurity elements, defects are introduced inside the semiconductor to become a recombination center of photogenerated carriers, thereby reducing the separation efficiency of photogenerated carriers.

Polar materials have a noncentrosymmetric spatial structure, in which positive and negative charge centers do not coincide, resulting in spontaneous polarization.[9] The advantages of the internal polarized electric field generated by spontaneous polarization present the following three aspects, namely, the internal polarized electric field generated by spontaneous polarization exists in the entire material and its range of action is large; thus, the stronger the electric field strength is; the fewer carrier recombination centers there are.[10] Therefore, the internal polarized electric field in polar material can more effectively promote the separation of the photogenerated carriers. Therefore, more and more scholars have explored polar materials, internal field mechanisms, and their functionalities. According to reports, $Ag_9(SiO_4)_2NO_3$,[11] $Ag_6Si_2O_7$,[12] $Bi_2O_2(OH)(NO_3)$,[13] $Bi_2O_2[BO_2(OH)]$,[14] Bi_2MoO_6,[15] $Bi_4V_2O_{11}$,[16] $NaNbO_3$,[17] $BaNbO(IO_3)_5$,[18] and so on exhibit significant photocatalytic activity. In these novel photocatalysts, owing to the stereochemically active of $6s^2$ lone pair of Bi^{3+} ions, Bi-based polar materials show outstanding spontaneous polarization effects.[19]

On the other hand, BiOI is considered as a new type of photocatalyst, due to its unique layered crystal structure.[20] Mi et al.[21] used a simple hydrothermal process to synthesize BiOI nanosheets and found that the samples have strong photocatalytic activity for degrading rhodamine B, methyl orange (MO), and phenol. However, the BiOI band gap is relatively small, resulting in a high recombination rate of photogenerated electron hole pairs. Recently, another polar photocatalytic material, $BiOIO_3$, which has the similar layered crystal structure with BiOI as shown in Figure 1, was synthesized.[22] $BiOIO_3$ also exhibits a layered structural topology composed of $(Bi_2O_2)^{2+}$ and $(IO_3)^-$ layers, which is very similar to that of BiOI. The only difference between them is that double I^- layers have become double $(IO_3)^-$ layers in $BiOIO_3$. The IO_3 triangular pyramid structure is asymmetric. Thus, the centers of positive charges and negative charges are not coinciding together, resulting residual dipole distance stacking to give $BiOIO_3$ a large macro polarity.[23] Wang et al.[24] have reported that the polarity of $BiOIO_3$ can effectively inhibit the recombination of electron−hole pairs. However, the relationship between IO_3 pyramid and macro polarity, and the intrinsic mechanism of this polarity-enhanced photocatalytic performance in $BiOIO_3$, has not been studied in depth. Hence, in this study, BiOI will be used as a reference comparison, and the combination of density functional theory (DFT) calculations with experiments will allow us to systematically elaborate the spontaneous polarization effects of $BiOIO_3$ as an efficient photocatalyst.

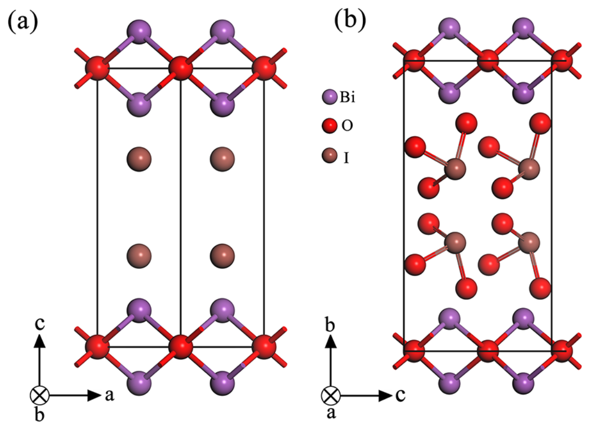

Figure 1. Crystal structure models of (a) BiOI and (b) $BiOIO_3$.

2. EXPERIMENTAL SECTION

2.1. Preparation of Sample. All of the chemicals used in the experiment were analytical grade reagents and were used without further purification. $BiOIO_3$ and BiOI samples are prepared by using a simple hydrothermal process. $Bi(NO_3)_3 \cdot 5H_2O$ and KIO_3 were used as the sources of Bi and IO_3, which are environmentally friendly and inexpensive. The $BiOIO_3$ sample was synthesized as follows. First, 1 mmol of Bi $(NO_3)_3 \cdot 5H_2O$ was dissolved in 40 mL of deionized water to form a suspension after constant stirring. Then, 1 mmol of KIO_3 was added into the suspension under vigorous stirring. The mixture was transferred into 100 mL Teflon-lined stainless steel autoclaves. The aqueous suspension was hydrothermally heated at a temperature of 150 °C. After they were heated for 5 h, the samples naturally

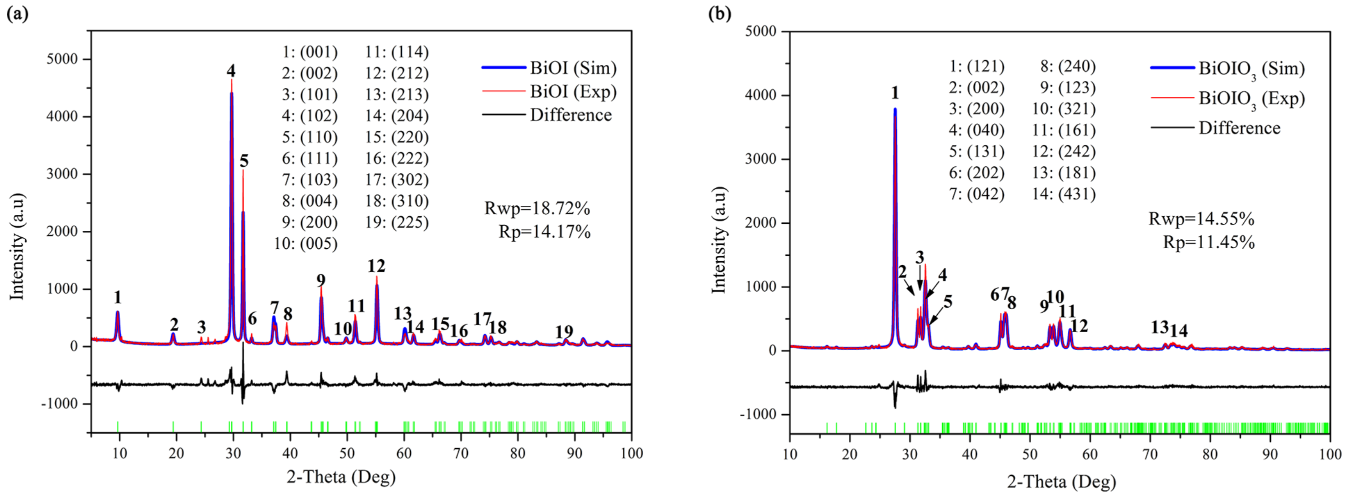

Figure 2. Power XRD patterns and results of Rietveld refinement of (a) BiOI and (b) $BiOIO_3$ synthesized by a hydrothermal method.

cooled to room temperature. Afterward, all generated samples were obtained by centrifuging them, filtering them, and rinsing them with deionized water and ethanol for four times. Finally, the samples were dried at 60 °C for 12 h. For comparison, BiOI was also prepared by the same simple hydrothermal process, in which KI was used instead of KIO_3.

2.2. Characterization. The crystal structure and phase purity of the samples was determined by X-ray diffraction (XRD, Bruker D8 Advance, Germany) using Cu Kα radiation, and the scanning range was 10−100° (2θ). The BET specific surface area of the samples was examined by the nitrogen adsorption−desorption (Micromeritics ASAP 2460, USA) method. The morphologies and structures of as-prepared samples were observed by scanning electron microscopy (SEM, S-4800 Hitachi, Japan), and the diffuse reflectance absorption spectra (DRAS) were obtained with a UV/vis spectrophotometer (UV-3900H, Hitachi, Japan).

2.3. Photocatalytic Degradation Testing. The photocatalytic activity of the $BiOIO_3$ and BiOI samples was evaluated by photocatalytic degradation of methyl orange (MO) under simulated solar-light irradiation (Xe Lamp, 300 W). Next, 0.2 g of as-prepared catalysts was stirred and dispersed in 200 mL of MO solutions (1 g/L) in a quartz reactor. Prior to irradiation, the suspensions were magnetically stirred in the darkness for 30 min to allow an adsorption−desorption equilibrium. After that, 5 mL of the liquid was sampled at every 10 min interval and then centrifuged to remove solid catalyst. The concentration of MO was determined by recording the characteristic absorption spectra on a UV−vis spectrophotometer.

The catalyst's lifetime is an important parameter of the photocatalytic process, so it is essential to evaluate the stability of photocatalyst for practical application. The recycling experiments on $BiOIO_3$ sample were carried out under the same reaction conditions. After every 40 min of photocatalytic degradation, the separated photocatalysts were washed with deionized water and then dried. Next, 200 mL of MO solutions (1 g/L) were readded to the quartz reactor; light was added, and the experiment was repeated four times.

2.4. Active Species Trapping Testing. For the purpose of detecting the active substances that play crucial roles in the photocatalytic process, radical trapping experiments have been carried out. Ethylene diamine tetraacetic acid disodium salt (EDTA-2Na, 1 mmol), *p*-benzoquinone (BQ, 1 mmol), and isopropanol (IPA, 1 mmol) were introduced in the degradation system to capture holes (h^+), superoxide radicals ($\bullet O_2^-$), and hydroxyl radicals ($\bullet OH$), respectively.[25−27]

2.5. Photoelectrochemical Testing. The transient photocurrent response, EIS, cyclic voltammetry curves, and Mott−Schottky curves were measured on an electrochemical system (ModuLab XM PhotoEchem, Solartron Analytical, England) with 0.1 M Na_2SO_4 solution as the electrolyte. A saturated calomel electrode and platinum (Pt) electrode were used as the reference electrode and the counter electrode, respectively. The sample film prepared on the FTO conductive glass was the working electrode and was prepared by a screen printing method. The printing slurry was prepared by mixing and grinding a sample (0.1 g), ethyl cellulose, lauric acid and pinealol according to the designed proportion. Subsequently, the obtained slurry was subjected to screen printing on a 13 mm × 14 mm FTO glass to form a film, which was placed in a muffle furnace and quenched at 400 °C for 2 h. The measurements are carried under simulated solar-light irradiation (Xe lamp, 300 W). The illuminated surface area was 4 cm^2, and the applied voltage was 0.2 V.

2.6. Computational Methods. All of the calculations were performed by using DFT software package of QuantumATK, in which the eigenfunctions of the Kohn−Sham Hamiltonian are expanded in a linear combination of atomic orbitals (LCAO). The basis sets were chose as pseudopotential SG15. The exchange-correlation interaction was treated by the meta-GGA method that is predefined by the function of TB09LDA. The density mesh cutoff was set as 200 hartree, in which the occupation method was chose as Fermi−Direc method with broadening of 25 meV. The Monkhorst−Pack scheme of k-points grid sampling was set as 19 × 19 × 3. The energy tolerance for self-consistent filed iteration was set as 0.0001 hartree in the algorithm of PulayMixer. The optimizer method of LBFGS was chosen for optimized geometry. Its convergence criteria were set as 0.05 eV/Å for force tolerance, 0.1 GPa for stress error tolerance, and 0.2 Å for maximum step size. During geometry optimization, the lattice vectors, space group, and Bravais lattice type were freely relaxed.

3. RESULTS AND DISCUSSION

3.1. Physical Characterization. The powder X-ray powder diffraction (XRD) patterns of as-prepared BiOI and $BiOIO_3$ samples are shown in Figure 2. First of all, the characteristic diffraction peaks of BiOI (Figure 2(a)) and $BiOIO_3$ (Figure 2(b)) accord well with the database of JCPDS file 10-0445 and ICSD no. 262019, respectively, demonstrating the pure phase of BiOI and $BiOIO_3$. No other peaks are found, suggesting the high purity and crystallinity of the samples. In addition, the powder XRD patterns of as-prepared BiOI and $BiOIO_3$ samples were refined. In Figure 2, the red curve is the experimental value, the blue curve is the analog value, and the black curve is the difference between the two. It can be seen the experimental values and the simulated values agree very well. In addition, the lattice constant obtained from Rietveld refinement is listed as the following. For BiOI, $a = b = 4.0422$ Å, $c = 9.8113$ Å; for $BiOIO_3$, $a = 5.6891$ Å, $b = 11.2521$ Å, $c =$

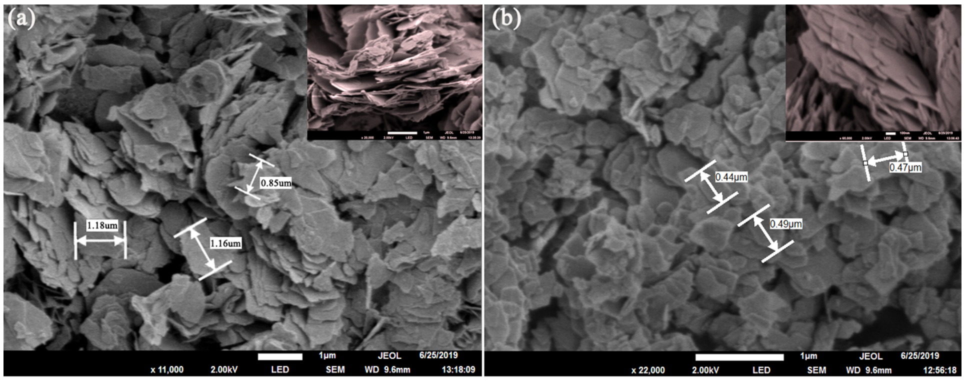

Figure 3. SEM images of (a) BiOI and (b) $BiOIO_3$ synthesized by a hydrothermal method.

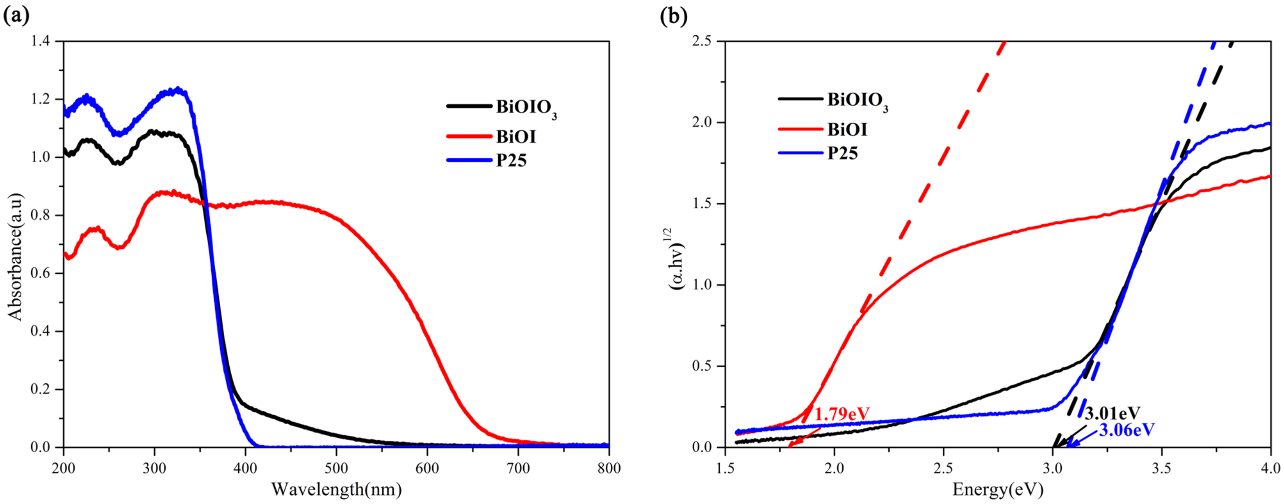

Figure 4. (a) UV−vis diffuse reflectance absorption spectra. (b) Band gaps of BiOI and $BiOIO_3$ estimated by the Tauc plot method.

5.7861 Å. After crystal structural optimization in DFT calculations, the lattice constant was obtained as follows. For BiOI, $a = b = 3.9915$ (3.9738) Å, $c = 9.1501$ (9.3722) Å; for $BiOIO_3$, $a = 5.6596$ (5.5396) Å, $b = 11.0502$ (11.0793) Å, $c = 5.7411$ (5.6434) Å, in which the corresponding measured values in the PDF card are provided in parentheses. By comparing the above three groups of lattice constants, one can find that they are very close. These results further demonstrate that the synthesized BiOI and $BiOIO_3$ samples are pure phases.

The particle size and morphology of BiOI and $BiOIO_3$ products were observed by the field emission SEM. As shown in Figure 3, both BiOI and $BiOIO_3$ samples show clear lamellar morphology, which is very similar to those of other $(Bi_2O_2)^{2+}$ layer-containing compounds.[28] This is the unique feature of layered compounds, which have been reported previously in the literature to easily synthesize similar morphologies. In the case of the BiOI sample, the width is estimated to be ∼1.1 μm, and the thickness is estimated to be ∼40 nm, as shown in Figure 3(a). Compared with BiOI sample, the $BiOIO_3$ sample shows a more uniform and smaller size morphology. As shown in Figure 3(b), the $BiOIO_3$ sample presents a flake stack morphology, which has an average width around ∼0.5 μm. It is important that the thickness of the $BiOIO_3$ sample is also estimated to ∼40 nm. And, the specific surface area of the pristine BiOI and $BiOIO_3$ was measured, which was determined to be 2.583 and 11.280 $m^2\ g^{-1}$, respectively. There is a certain difference in the specific surface area of BiOI and $BiOIO_3$, which may be due to their special interlayer messy staggered stack structure. In the field of photocatalysis, the nanoscale platelet-like morphology has the special advantage of a shorter carrier diffusion distance, which enables the carrier to reach the reactive site on the surface within its lifetime.[29] Furthermore, the thickness of the layered photocatalytic material is also an important factor affecting the photocatalytic performance.[30] In the present work, since $BiOIO_3$ and BiOI have the same morphology and longitudinal size, it can be assumed that these factors should contribute the same to their photocatalytic performances.

3.2. UV−Vis Light Absorption Properties. The UV−vis diffuse reflectance absorption spectra (DRAS) of BiOI and $BiOIO_3$ are displayed in Figure 4(a). It shows that the absorption edges of BiOI and $BiOIO_3$ were located at approximately 650 and 400 nm, respectively. This observation clearly indicates that BiOI is a visible-light-driven photocatalyst, while $BiOIO_3$ is a UV-light-driven photocatalyst. This is a major obstacle to the development of $BiOIO_3$-based photocatalysts and a direction to be broken in the future. In semiconductors, the square of the absorption coefficient (α) is linear with photon energy for direct optical transitions in the absorption edge region, whereas the square root of the absorption coefficient is linear with photon energy for indirect transitions.[31] Data plots of $(\alpha h\nu)^{1/2}$ versus photon energy in the absorption edge region for BiOI and $BiOIO_3$ shown in Figure 4(a) are nearly linear, indicating the absorption edge of BiOI and $BiOIO_3$ is caused by indirect transitions. Band gaps of the two compounds are determined by optical absorption

DOI: 10.1021/acs.inorgchem.9b02328
Inorg. Chem. XXXX, XXX, XXX−XXX

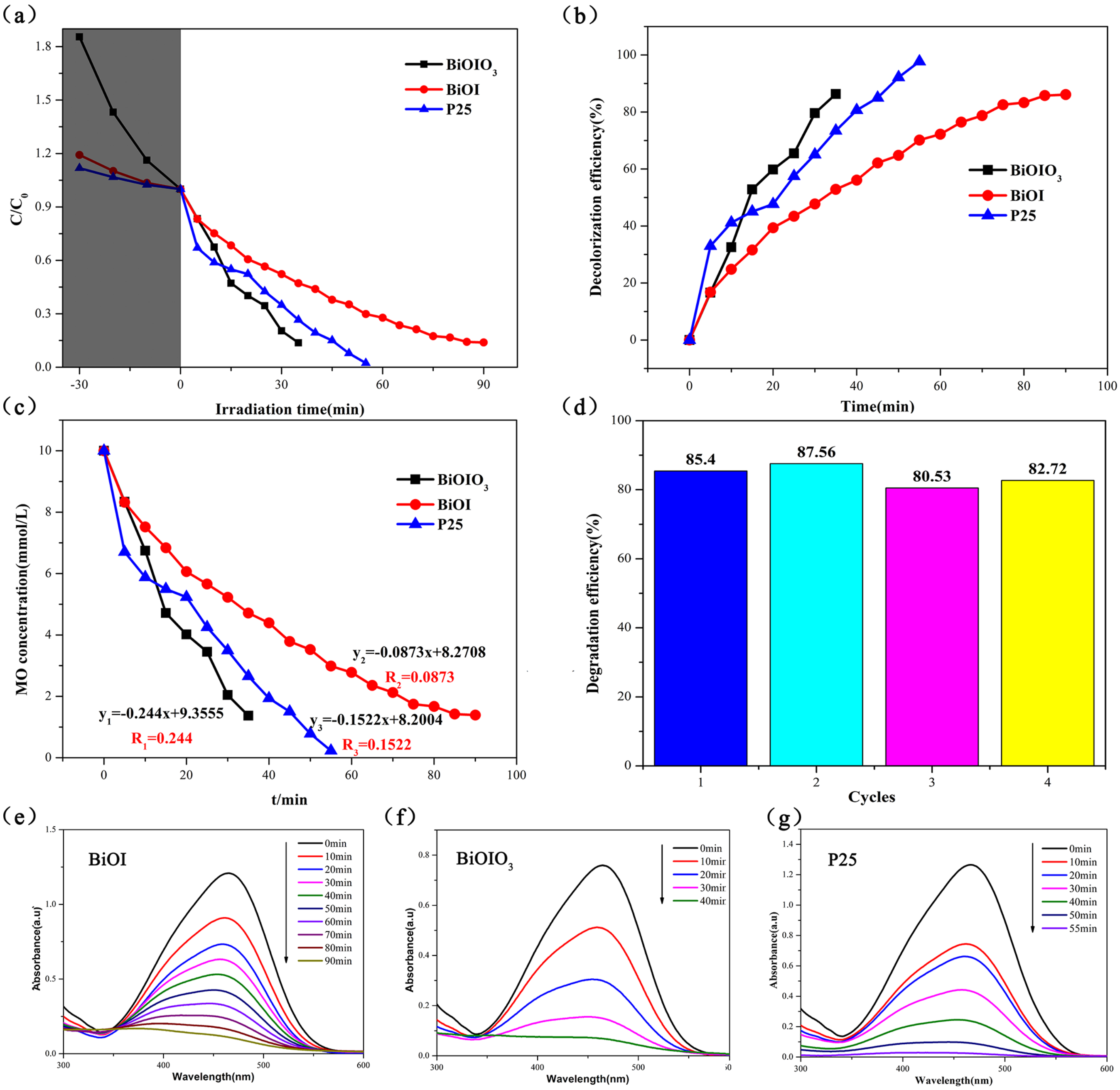

Figure 5. (a) Photocatalytic degradation rate, (b) decolorization efficiency, and (c) photocatalysis performance index of MO for $BiOIO_3$ powder, which are compared with BiOI and P25 powder. (d) Cycling runs in the photocatalytic degradation of MO in the presence of $BiOIO_3$ samples. Absorbance spectrum of MO solution in the presence of the as-prepared (e) BiOI, (f) $BiOIO_3$, and (g) P25.

near the band edge by the following equation: $\alpha(h\nu) = A(h\nu - E_g)^{n/2}$, where α, $h\nu$, A, and E_g are the optical absorption coefficient, photonic energy, proportionality constant, and band gap, respectively.[32] In this equation, n determines the type of the transition in a semiconductor (n = 1, direct absorption; n = 4, indirect absorption). By applying n = 4, we can determine the indirect band gap of BiOI and $BiOIO_3$ from the plot of $(\alpha h\nu)^{1/2}$ versus photon energy, as presented in the Figure 4(b). By extrapolating the straight line to the x-axis in this plot, we estimated the E_g of BiOI and $BiOIO_3$ to 1.79 and 3.01 eV, respectively. Among them, the band gap value of $BiOIO_3$ is close to that of P25 (3.06 eV).

However, the band gap of $BiOIO_3$ is larger than the band gap of BiOI, resulting in a large difference in the light absorption range. The most fundamental reason for this is that the interaction between atoms in the Bi_2O_4 layer has changed. For the Bi_2O_4 layer in BiOI, the distances between Bi—Bi and Bi—O are 3.968 and 2.331 Å, respectively. Compared with $BiOIO_3$, the distances between Bi—Bi and Bi—O in the Bi_2O_4 layer are 3.777 and 2.304 Å, respectively. Obviously, due to the introduction of the IO_3 pyramid, the bond length between the atoms of the Bi_2O_4 layer in the $BiOIO_3$ structure is shortened and the interaction becomes stronger, such that the conduction band moves up and the band gap becomes larger.

3.3. Photocatalytic Degradation Testing. The photocatalytic activities of BiOI and $BiOIO_3$ samples were evaluated by photocatalytic degradation of MO under UV—vis light irradiation under refrigeration of condensed water to 10 °C.

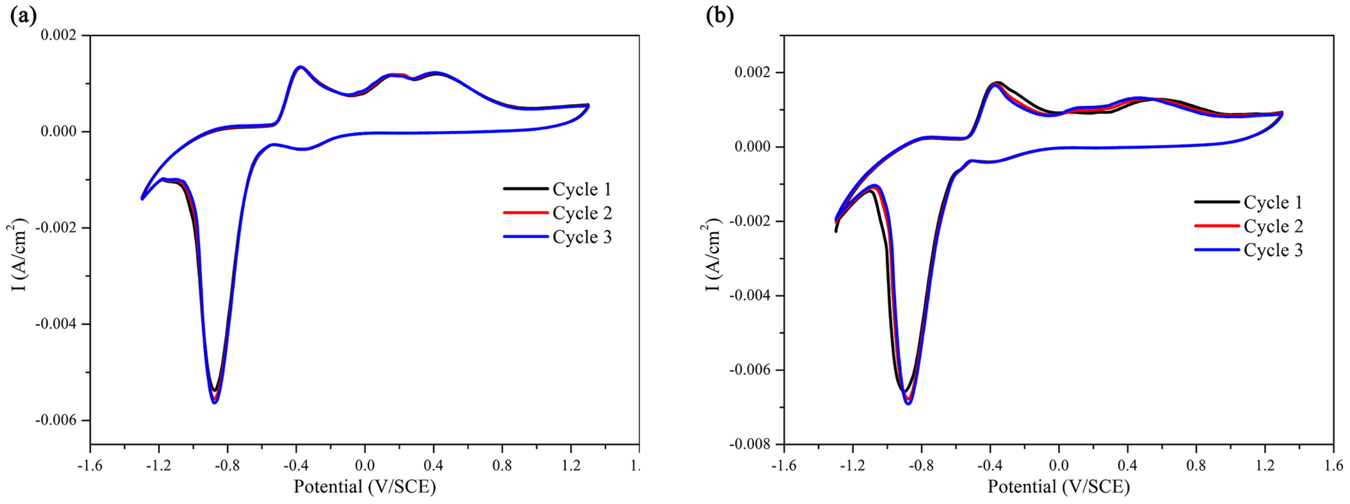

Figure 6. Cyclic voltammetry curve of (a) BiOI and (b) $BiOIO_3$ synthesized by a hydrothermal method.

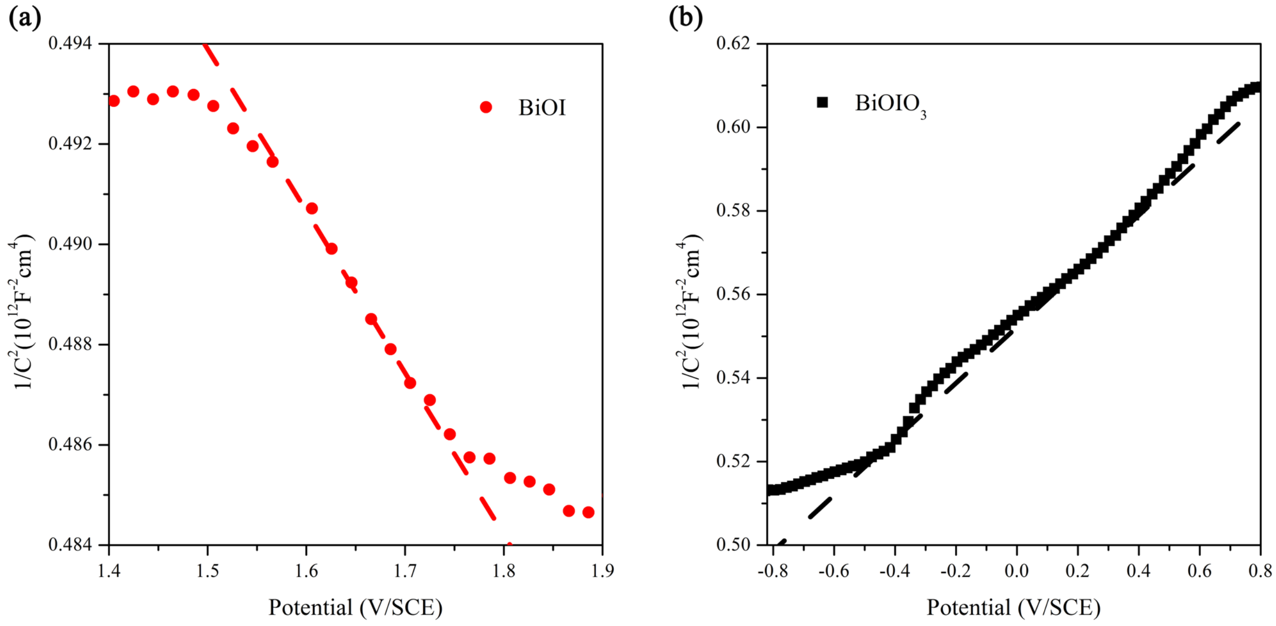

Figure 7. Mott–Schottky curves of (a) BiOI and (b) $BiOIO_3$ synthesized by a hydrothermal method.

The degradation efficiencies are defined as C/C_0, in which C and C_0 represent the remnant and initial concentration of MO, respectively. MO is quite stable, and its self-photolysis is negligible. Figure 5(a)–5(c) illustrate the photocatalytic performances [(a): photocatalytic degradation rate; (b): decolorization efficiency; (c): photocatalysis performance index] of $BiOIO_3$ powder, which are compared with those of BiOI and P25 powder. $BiOIO_3$ shows superior photocatalytic performance relative to BiOI in the degradation rate, decolorization rate, and photolysis index. Even more surprising is that $BiOIO_3$ also has a better photocatalytic performance than P25. At the same time, as discussed in the previous DRAS measurements, the light absorption range of $BiOIO_3$ is much smaller than that of BiOI and almost the same as that of P25. On the one hand, $BiOIO_3$ and BiOI have a similar layered crystal structure. $BiOIO_3$ and P25 have identical spectral response characteristics. On the other hand, the crystal structure of BiOI and P25 determines that they have no internal polarized electric field. Combining this evidence, the excellent photocatalytic performance of $BiOIO_3$ can be preliminarily identified as its own internal polarized electric field. To evaluate the stability of samples in the photocatalytic reaction, $BiOIO_3$ was reclaimed and re-examined for four extra cycles as shown in Figure 5(d). $BiOIO_3$ did not exhibit any significant loss of activity. It implies that $BiOIO_3$ has long-term stability. The MO concentrations versus the reaction time and absorbance curves for these photocatalysts are plotted in Figure 5(e)–5(g) [(e): BiOI; (f): $BiOIO_3$; (g): P25]. It shows that MO was almost photocatalytically degraded by BiOI, $BiOIO_3$, and P25 in 90, 40, and 55 min, respectively. These results demonstrate that $BiOIO_3$ can be used as an efficient, stable, and low-cost alternative photocatalyst.

3.4. Photoelectrochemical Properties and Photocatalytic Mechanism.

To obtain insight into the uncommon photocatalytic activity trend, the charge separation and transfer behaviors were investigated by a string of photoelectrochemical characterizations. First, the cyclic voltammetry trend of BiOI as shown in Figure 6(a) and $BiOIO_3$ as shown in Figure 6(b) are

DOI: 10.1021/acs.inorgchem.9b02328
Inorg. Chem. XXXX, XXX, XXX–XXX

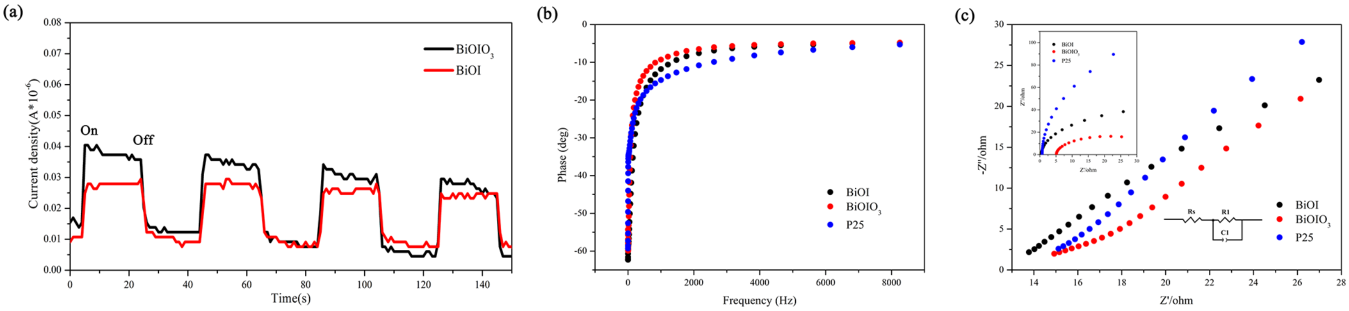

Figure 8. (a) Transient photocurrent responses, (b) Bode-phase spectra, and (c) EIS Nyquist plots of $BiOIO_3$, BiOI, and P25.

very similar. The peak intensity of the reduction peak (downward peak) is greater than the peak intensity of the oxidation peak (upward peak), indicating that the two are more susceptible to reduction, and both show good redox ability. At the same time, the volt−ampere curve of the three cycles showed only a slight change, indicating that the two have good stability. This is consistent with the results of the degradation MO cycle experiment in Figure 5(d).

In this article, the semiconductor types and flat-band potentials of BiOI and $BiOIO_3$ were determined by Mott−Schottky (M-S) methods.[33,34] It is well-known that the slope of linear $1/C^2$ versus potential curves is positive for n-type semiconductors and negative for p-type semiconductors.[35,36] The slope of linear $1/C^2$-potential curves of $BiOIO_3$ as shown in Figure 7(a) and BiOI Figure 7(b) are separately positive and negative, indicating that BiOI and $BiOIO_3$ are p-type and n-type semiconductors, respectively. By calculating the values of the abscissa axis-intercept with extrapolation to $1/C^2 = 0$, the flat potentials of $BiOIO_3$ and BiOI are separately determined to be −0.81 and 1.81 V, versus the saturated calomel electrode (SCE), which is in good agreement with the reported values.[37] They amount to −0.613 and 2.007 V, respectively, versus the normal hydrogen electrode (NHE).

The transient photocurrent response can indicate the generation and separation efficiency of photoexcited charge carriers. As revealed by Figure 8(a), the two photoelectrodes show a stable photocurrent response, and $BiOIO_3$ produces a current density of 0.025 $\mu A/cm^2$ with the light on, which is 1.5 times that of BiOI (0.017 $\mu A/cm^2$). Evidently, $BiOIO_3$ possesses a much higher charge separation efficiency. Figure 8(b) displays the Bode-phase spectra, which can reflect the lifetime of injected electrons that is highly correlated with the frequency (f). According to the equation $\tau = 1/(2\pi f)$,[38] the lifetime of injected electrons in $BiOIO_3$ (47.4×10^{-6} s) is estimated to be approximately 1.9 times and 3.1 times higher than that of BiOI (24.9×10^{-6} s) and P25 (15.5×10^{-6} s), respectively. It can be seen that the injected electron lifetime of $BiOIO_3$ is much longer than that of BiOI and P25. Furthermore, in order to detect the interfacial transfer efficiency of the catalysts, electrochemical impedance spectroscopy (EIS) was measured. Figure 8(c) shows Nyquist EIS plots of $BiOIO_3$ and BiOI with irradiation of visible light. It is clear that $BiOIO_3$ has a smaller arc radius than BiOI, indicating the higher charge mobility at the interface between $BiOIO_3$ and the electrolyte. The EIS that is obtained by the Zview software simulation equivalent circuit processing, as shown in the inset of Figure 8(c), also verifies this result. Overall, the results of multiple spectra indicate that charge separation and transfer efficiencies play significant roles in the photocatalytic reaction of $BiOIO_3$, which makes $BiOIO_3$ have higher photocatalytic activity. It is further proved that the internal polarized electric field can enhance the charge separation and transmission efficiency, so that the photocatalytic performance of the polar material $BiOIO_3$ is better than that of BiOI and P25.

To speculate the photocatalytic mechanism, radical trapping experiments are performed to capture the reactive species generated in the degradation process. As shown in Figure 9, the MO degradation rate was almost not influenced by the addition of isopropyl alcohol (IPA, a scavenger of •OH), excluding the effect of •OH. By contrast, both the p-benzoquinone (BQ, a scavenger of $•O_2^-$) and ethylene diamine tetraacetic acid disodium salt (EDTA-2Na, a scavenger of h^+) have significant impediment in MO degradation, revealing that $•O_2^-$ and h^+ are the critical active species.

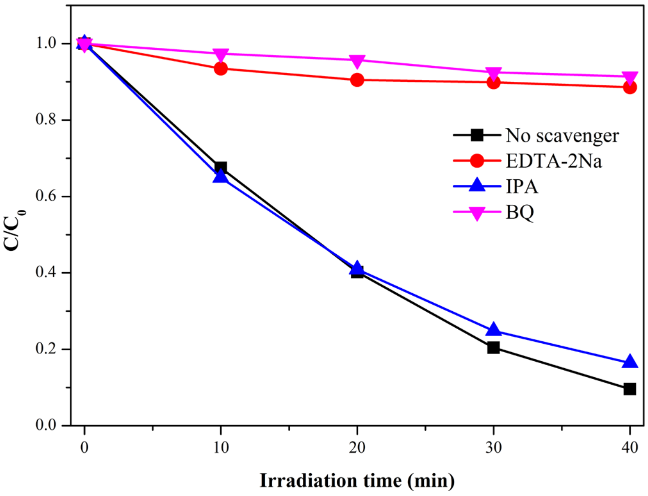

Figure 9. Photocatalytic degradation curve of MO over $BiOIO_3$ alone and with the addition of EDTA-2Na, IPA, and BQ.

3.5. Electronic Structure of BiOI and $BiOIO_3$.

The calculated electronic structures (i.e., band structure and density of states) of BiOI and $BiOIO_3$ are illustrated in Figure 10. First of all, the obtained band gap values of BiOI as shown in Figure 10(a) and of $BiOIO_3$ as shown in Figure 10(b) are 2.03 and 2.91 eV, respectively, which are very consistent with above DRAS measurements and previous reports. So, the meta-GGA functional within the LCAO method can overcome the well-known underestimated band gap by GGA functional within the plane wave method.[39] In fact, there are little differences between DRAS measurements and DFT calculations; the main reasons can be ascribed to the following aspects: (1) the

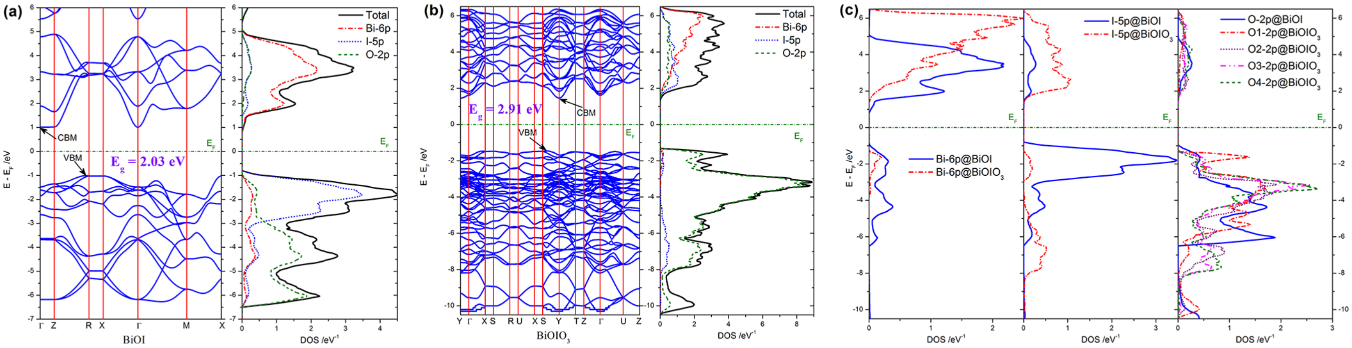

Figure 10. Band structures and total density of states of (a) BiOI and (b) $BiOIO_3$. (c) The corresponding local density of states in BiOI and $BiOIO_3$.

defects are unavoidable in samples prepared by the chemical solution method and (2) DFT calculations only consider the properties of the ground state at absolute zero. As shown in Figure 10(a), in the case of BiOI, the valence band maximum (VBM) is located on the ZR line, while the conduction band minimum (CBM) is located at Γ point. As shown in Figure 10(b), in the case of $BiOIO_3$, the VBM is located on the YS line, while the CBM is located at Y point. This result indicates that both BiOI and $BiOIO_3$ are the indirect band gap semiconductors, which is confirmed above discussions about Tacu plot method in Figure 4(b). The symmetry group of BiOI is *P*4/*nmm* (no. 129), while the symmetry group of $BiOIO_3$ is Pca2_1 (no. 29). In other words, BiOI has higher symmetry, so its band structure shows higher degeneracy and dispersion.

To clearly understand the contribution of atom and orbital to the electronic states, the total and local density of states (DOS) are also provide in Figure 10. As described in Figure 10(a) and Figure 10(c), it is found that the conduction band (CB) of BiOI mostly consists of Bi6p states; the upper valence band (VB) is mainly composed by I-5p states, and the lower VB is mainly composed by O-2p states. In the whole range of VB and CB of BiOI, there are slight hybridized states between O-2p states and Bi6p or I-5p states. As described in Figure 10(b) and Figure 10(c), it is found that the lower CB of $BiOIO_3$ is mainly composed by I-5p states, and the upper CB is mainly composed by Bi6p states; the VB mostly consists of O-2p states. In the whole range of CB $BiOIO_3$, there are obvious hybridized states between O-2p states and Bi6p or I-5p states. These results are consistent with previous literature on $BiOIO_3$.[20,40] Although BiOI and $BiOIO_3$ have similar layered structures, their electronic structures show different compositions. This is mainly due to the different interactions between layers. In the case of BiOI, the Bi_2O_2 layers are connected by the van der Waals interaction of I^- ions; while in the case of $BiOIO_3$, the Bi_2O_2 layers are connected by the bridging valence interaction of IO_3^- group. Furthermore, there are three kinds of oxygen atoms in $BiOIO_3$, i.e., the O1 atoms form the Bi_2O_2 layers, the O2 atoms bridging the BiO_6 and IO_3 pyramids, and the O3/O4 atoms forming the terminal atoms of IO_3 pyramids, as shown in Figure 11.[24] These three kinds of oxygen atoms show different contributions of the composition of VB. According to above analysis, the photogenerated holes are mainly located on the O-2p states, while the photogenerated electrons are mainly located on the Bi6p and I-5p states.

In order to more clearly describe the separation and transfer process of photogenerated electron−hole pairs in $BiOIO_3$, the intrinsic mechanism is further analyzed. The Bader method is used to calculate the charge distribution, and the results are as follows: +1.769 e at Bi atom, −0.506 e at I atom, and −1.263 e at O atom in the case of BiOI and +2.168 e at Bi atom, +2.567e at I atom, −1.340 e at O1 atom, −1.138 e at O2/O3 atom, and −1.120 e at O4 atom in the case of $BiOIO_3$. First of all, the I atom obtains electrons in BiOI, while the I atom contributes electrons in $BiOIO_3$. Second of all, the O atom located at different sites will obtain different electrons in $BiOIO_3$. The asymmetry of spatial atom distribution and the uneven charge distribution IO_3 groups are the two key factors for generating the internal polarized electric field in $BiOIO_3$. In previous works, the internal polarized electric field has often been described by the dipole moment of polyhedron.[41−43] Therefore, it is easy to estimate the internal polarized electric field (~1.5 × 10^{10} V/m) in $BiOIO_3$, according to the optimized geometrical configurations and charge distributions. The calculation uses the following formula: $E = \sigma/\varepsilon_r(0)$ (where σ is the surface charge density, and $\varepsilon_r(0)$ is the static dielectric constant). The value of σ could be determined by the Mulliken population analysis, and the value of $\varepsilon_r(0)$ is determined by the optical properties calculations. Although previous literature reports have reported that BiOI also has internal polarized electric fields, its internal polarized electric fields are arranged alternating along the *c*-axis with equal magnitude and opposite direction, and the final effective electric field is equal to zero. On the opposite, the internal polarized electric fields in $BiOIO_3$ can be accumulated along the *c*-axis, due to the same polarization direction of IO_3 groups. In this part of the theoretical calculations, the existence of a polar electric field in $BiOIO_3$ is confirmed and its origin is elucidated. Simultaneously, it fully reveal the root cause of the higher

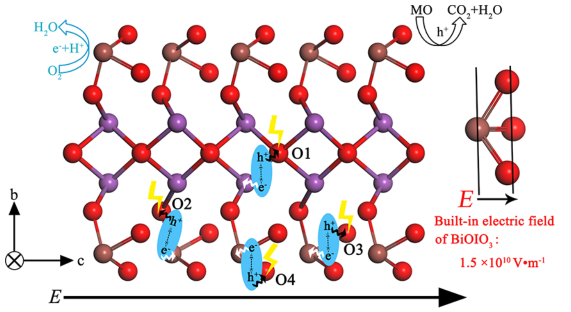

Figure 11. Schematic diagram of the separation mechanism of photogenerated electron−hole pairs and the estimated internal polarized electric field in $BiOIO_3$.

photocatalytic performance of $BiOIO_3$ in the above experimental test results.

The underlying mechanism of enhanced photocatalytic performace of $BiOIO_3$ is summarized in Figure 11. With the internal polarized electric field in $BiOIO_3$, the photogenerated electrons on O atoms can be effectively transferred to Bi/I atoms, while the photogenerated holes remain on O atoms. Then, the separated electrons and holes will be fast transfer to the surface of $BiOIO_3$ sample along opposite directions. Finally, the photo-oxidation would occur at the O sites on the surface, and the photoreduction would occur at the Bi/I sites. Therefore, the internal polarized electric field is the key factor to enhance the photocatalytic performances of $BiOIO_3$, compared with BiOI and P25.

4. CONCLUSIONS

In summary, a layered polar compound of $BiOIO_3$ was synthesized from $Bi(NO_3)_3{\cdot}5H_2O$ and KIO_3 by using a hydrothermal method. The as-prepared $BiOIO_3$ sample is a pure phase and exhibits clear lamellar morphology. Combined with optical measurements and DFT calculations, $BiOIO_3$ is an indirect gap semiconductor with a band gap of 2.91 eV. The photocatalytic degradation testing indicates that $BiOIO_3$ shows excellent photocatalytic performance for methyl orange degradation under UV−vis light irradiation, which is much better than its counterpart of BiOI and P25. And, it also presents long-term stability. Additionally, superoxide radicals ($\bullet O_2^-$) and holes (h^+) are produced during the degradation process. The photoelectrochemical measurements demonstrate that $BiOIO_3$ has a higher separation rate of photogenerated electron−hole pairs. The DFT calculations also prove that there are internal polarized electric fields in $BiOIO_3$ along the *c*-axis, which is the root to the asymmetry of spatial atom distribution and the uneven charge distribution IO_3 groups. The photogenerated electrons and holes were gathered mainly on Bi/I and O atoms, respectively. Under the action of the internal polarized electric field ($\sim 1.5 \times 10^{10}$ V/m), the photogenerated electrons and holes could transfer along opposite directions, which facilitates the separation rate of photogenerated electron−hole pairs. Thus, the higher photocatalytic efficiency of $BiOIO_3$ is caused by the internal polarized electric field, in comparison with BiOI and P25.

It is worth noting that the large macroscopic polarity is mainly attributed to the alignment of the lone-pair-containing IO_3 polyhedra. Therefore, further research on the polar groups, such as doping, atomic substitution, etc., can be carried out in subsequent work, thereby fully exerting the promoting effect of the inner polar field on the photocatalytic performance. In addition, the correspondence between the internal polar electric field generated by the spontaneous polarization of polar materials and the photocatalytic performance is worthy of further investigation.

■ ASSOCIATED CONTENT

Accession Codes

CCDC 1946651 and 1946712 contain the supplementary crystallographic data for this paper. These data can be obtained free of charge via www.ccdc.cam.ac.uk/data_request/cif, or by emailing data_request@ccdc.cam.ac.uk, or by contacting The Cambridge Crystallographic Data Centre, 12 Union Road, Cambridge CB2 1EZ, UK; fax: +44 1223 336033.

■ AUTHOR INFORMATION

Corresponding Author

*E-mail: zzy@kmust.edu.cn.

ORCID

Zong-Yan Zhao: 0000-0001-8953-3150

Notes

The authors declare no competing financial interest.

■ ACKNOWLEDGMENTS

The authors would like to acknowledge financial support from the National Natural Science Foundation of China (11964015) and the 18th Yunnan Province Young Academic and Technical Leaders Reserve Talent Project (2015HB015).

■ REFERENCES

(1) Lou, Z.; Wang, P.; Huang, B.; Dai, Y.; Qin, X.; Zhang, X.; Wang, Z.; Liu, Y. Enhancing Charge Separation in Photocatalysts with Internal Polar Electric Fields. *Chemphotochem* **2017**, *1* (5), 136−147.

(2) Ling, Z.; Yang, S.; Wang, W. Internal Electric Fields within the Photocatalysts. *Prog. Chem.* **2016**, *28* (4), 415−427.

(3) Grosso, D.; Boissière, C.; Smarsly, B.; Brezesinski, T.; Pinna, N.; Albouy, P. A.; Amenitsch, H.; Antonietti, M.; Sanchez, C. Periodically ordered nanoscale islands and mesoporous films composed of nanocrystalline multimetallic oxides. *Nat. Mater.* **2004**, *3* (11), 787−92.

(4) Li, H.; Sang, Y.; Chang, S.; Huang, X.; Zhang, Y.; Yang, R.; Jiang, H.; Liu, H.; Wang, Z. L. Enhanced Ferroelectric-Nanocrystal-Based Hybrid Photocatalysis by Ultrasonic-Wave-Generated Piezophototronic Effect. *Nano Lett.* **2015**, *15* (4), 2372−2379.

(5) Jiang, T.; Xie, T.; Zhang, Y.; Chen, L.; Peng, L.; Li, H.; Wang, D. Photoinduced charge transfer in ZnO/Cu_2O heterostructure films studied by surface photovoltage technique. *Phys. Chem. Chem. Phys.* **2010**, *12* (47), 15476.

(6) Wang, X.; Xu, Q.; Li, M.; Shen, S.; Wang, X.; Wang, Y.; Feng, Z.; Shi, J.; Han, H.; Li, C. Photocatalytic overall water splitting promoted by an α-β phase junction on Ga_2O_3. *Angew. Chem., Int. Ed.* **2012**, *51* (52), 13089−13092.

(7) Zhao, W.; Guo, Y.; Wang, S.; He, H.; Sun, C.; Yang, S. A novel ternary plasmonic photocatalyst: ultrathin $g\text{-}C_3N_4$ nanosheet hybrided by $Ag/AgVO_3$ nanoribbons with enhanced visible-light photocatalytic performance. *Appl. Catal., B* **2015**, *165*, 335−343.

(8) Long, M.; Cai, W.; Wang, Z.; Liu, G. Correlation of electronic structures and crystal structures with photocatalytic properties of undoped, N-doped and I-doped TiO_2. *Chem. Phys. Lett.* **2006**, *420* (1), 71−76.

(9) Chen, F.; Huang, H.; Guo, L.; Zhang, Y.; Ma, T. The Role of Polarization in Photocatalysis. *Angew. Chem., Int. Ed.* **2019**, *58* (30), 10061−10073.

(10) Wang, Z.; Huang, B.; Dai, Y. Design and synthesis of highly reactive photocatalysts. *Materials China* **2017**, *36* (1), 7−16.

(11) Zhu, X.; Wang, Z.; Huang, B.; Wei, W.; Dai, Y.; Zhang, X.; Qin, X. Synthesis of $Ag_9(SiO_4)_2NO_3$ through a reactive flux method and its visible-light photocatalytic performances. *APL Mater.* **2015**, *3* (10), 104413.

(12) Lou, Z.; Huang, B.; Wang, Z.; Ma, X.; Zhang, R.; Zhang, X.; Qin, X.; Dai, Y.; Whangbo, M.-H. $Ag_6Si_2O_7$: a silicate photocatalyst for the visible region. *Chem. Mater.* **2014**, *26* (13), 3873−3875.

(13) Huang, H.; He, Y.; Li, X.; Li, M.; Zeng, C.; Dong, F.; Du, X.; Zhang, T.; Zhang, Y. $Bi_2O_2(OH)(NO_3)$ as a desirable $[Bi_2O_2]^{2+}$ layered photocatalyst: strong intrinsic polarity, rational band structure and {001} active facets co-beneficial for robust photooxidation capability. *J. Mater. Chem. A* **2015**, *3* (48), 24547−24556.

(14) Zhang, R.; Dai, Y.; Lou, Z.; Li, Z.; Wang, Z.; Yang, Y.; Qin, X.; Zhang, X.; Huang, B. Layered photocatalyst $Bi_2O_2[BO_2(OH)]$ nanosheets with internal polar field enhanced photocatalytic activity. *CrystEngComm* **2014**, *16* (23), 4931−4934.

(15) Chen, Y.; Yang, W.; Gao, S.; Zhu, L.; Sun, C.; Li, Q. Internal Polarization Modulation in Bi_2MoO_6 for Photocatalytic Performance Enhancement under Visible-Light Illumination. *ChemSusChem* **2018**, *11* (9), 1521−1532.

(16) Jiang, Z.; Liu, Y.; Li, M.; Jing, T.; Huang, B.; Zhang, X.; Qin, X.; Dai, Y. One-Pot Solvothermal Synthesis of $Bi_4V_2O_{11}$ as A New Solar Water Oxidation Photocatalyst. *Sci. Rep.* **2016**, *6*, 22727.

(17) Jiang, L.; Zhang, Y.; Qiu, Y.; Yi, Z. Improved photocatalytic activity by utilizing the internal electric field of polar semiconductors: a case study of self-assembled $NaNbO_3$ oriented nanostructures. *RSC Adv.* **2014**, *4* (7), 3165−3170.

(18) Sun, C. F.; Hu, C. L.; Xu, X.; Ling, J. B.; Hu, T.; Kong, F.; Long, X. F.; Mao, J. G. $BaNbO(IO_3)_5$: A New Polar Material with a Very Large SHG Response. *J. Am. Chem. Soc.* **2009**, *131* (27), 9486−7.

(19) Li, M.; Huang, H.; Yu, S.; Tian, N.; Zhang, Y. Facet, Junction and Electric Field Engineering of Bismuth-Based Materials for Photocatalysis. *ChemCatChem* **2018**, *10* (20), 4477−4496.

(20) Zhao, Z. Y.; Dai, W. W. Structural, electronic, and optical properties of Eu-doped BiOX (X = F, Cl, Br, I): a DFT+U study. *Inorg. Chem.* **2014**, *53* (24), 13001−13011.

(21) Mi, Y.; Zhou, M.; Wen, L.; Zhao, H.; Lei, Y. A highly efficient visible-light driven photocatalyst: two dimensional square-like bismuth oxyiodine nanosheets. *Dalton Trans.* **2014**, *43* (25), 9549−9556.

(22) Nguyen, S. D.; Yeon, J.; Kim, S. H.; Halasyamani, P. S. BiO(IO3): a new polar iodate that exhibits an aurivillius-type $(Bi_2O_2)^{2+}$ layer and a large SHG response. *J. Am. Chem. Soc.* **2011**, *133* (32), 12422−5.

(23) Huang, H.; Tu, S.; Zeng, C.; Zhang, T.; Reshak, A. H.; Zhang, Y. Macroscopic Polarization Enhancement Promoting Photo- and Piezoelectric-Induced Charge Separation and Molecular Oxygen Activation. *Angew. Chem., Int. Ed.* **2017**, *56* (39), 11860−11864.

(24) Wang, W.; Huang, B.; Ma, X.; Wang, Z.; Qin, X.; Zhang, X.; Dai, Y.; Whangbo, M. H. Efficient separation of photogenerated electron-hole pairs by the combination of a heterolayered structure and internal polar field in pyroelectric $BiOIO_3$ nanoplates. *Chem. - Eur. J.* **2013**, *19* (44), 14777−80.

(25) Huang, H.; Han, X.; Li, X.; Wang, S.; Chu, P. K.; Zhang, Y. Fabrication of Multiple Heterojunctions with Tunable Visible-Light-Active Photocatalytic Reactivity in BiOBr−BiOI Full-Range Composites Based on Microstructure Modulation and Band Structures. *ACS Appl. Mater. Interfaces* **2015**, *7* (1), 482−492.

(26) Huang, H.; Li, X.; Wang, J.; Dong, F.; Chu, P. K.; Zhang, T.; Zhang, Y. Anionic Group Self-Doping as a Promising Strategy: Band-Gap Engineering and Multi-Functional Applications of High-Performance CO_3^{2-}-Doped $Bi_2O_2CO_3$. *ACS Catal.* **2015**, *5* (7), 4094−4103.

(27) Huang, H.; Xiao, K.; He, Y.; Zhang, T.; Dong, F.; Du, X.; Zhang, Y. In situ assembly of $BiOI@Bi_{12}O_{17}Cl_2$ p−n junction: charge induced unique front-lateral surfaces coupling heterostructure with high exposure of BiOI {001} active facets for robust and nonselective photocatalysis. *Appl. Catal., B* **2016**, *199*, 75−86.

(28) Hao, L.; Huang, H.; Guo, Y.; Zhang, Y. Multifunctional $Bi_2O_2(OH)(NO_3)$ Nanosheets with {001} Active Exposing Facets: Efficient Photocatalysis, Dye-Sensitization, and Piezoelectric-Catalysis. *ACS Sustainable Chem. Eng.* **2018**, *6* (2), 1848−1862.

(29) Liu, Y.; Mi, X.; Wang, J.; Li, M.; Fan, D.; Lu, H.; Chen, X. Two-dimensional SnS_2 nanosheets exfoliated from an inorganic−organic hybrid with enhanced photocatalytic activity towards Cr(vi) reduction. *Inorg. Chem. Front.* **2019**, *6* (4), 948−954.

(30) Chen, F.; Huang, H.; Ye, L.; Zhang, T.; Zhang, Y.; Han, X.; Ma, T. Thickness-Dependent Facet Junction Control of Layered $BiOIO_3$ Single Crystals for Highly Efficient CO_2 Photoreduction. *Adv. Funct. Mater.* **2018**, *28*, 1804284.

(31) Zhang, K. L.; Liu, C. M.; Huang, F. Q.; Zheng, C.; Wang, W. D. Study of the electronic structure and photocatalytic activity of the BiOCl photocatalyst. *Appl. Catal., B* **2006**, *68* (3), 125−129.

(32) Cheng, H.; Huang, B.; Dai, Y.; Qin, X.; Zhang, X. One-Step Synthesis of the Nanostructured AgI/BiOI Composites with Highly Enhanced Visible-Light Photocatalytic Performances. *Langmuir* **2010**, *26* (9), 6618−6624.

(33) He, Z. Q.; Wang, D.; Fang, H. Y.; Chen, J. M.; Song, S. Highly efficient and stable $Ag/AgIO_3$ particles for photocatalytic reduction of CO_2, under visible light. *Nanoscale* **2014**, *6* (18), 10540.

(34) Huang, H.; He, Y.; Lin, Z.; Kang, L.; Zhang, Y. Two Novel Bi-Based Borate Photocatalysts: Crystal Structure, Electronic Structure, Photoelectrochemical Properties, and Photocatalytic Activity under Simulated Solar Light Irradiation. *J. Phys. Chem. C* **2013**, *117* (44), 22986−22994.

(35) He, Z. Q.; Wang, D.; Fang, H. Y.; Chen, J. M.; Song, S. Highly efficient and stable $Ag/AgIO_3$ particles for photocatalytic reduction of CO_2 under visible light. *Nanoscale* **2014**, *6* (18), 10540.

(36) Lee, K.; Ruddy, D. A.; Dukovic, G.; Neale, N. R. Synthesis, optical, and photocatalytic properties of cobalt mixed-metal spinel oxides $Co(Al_{1-x}Ga_x)_2O_4$. *J. Mater. Chem. A* **2015**, 3 (15), 8115−8122.

(37) Huang, H.; Xiao, K.; Liu, K.; Yu, S.; Zhang, Y. In Situ Composition-Transforming Fabrication of $BiOI/BiOIO_3$ Heterostructure: Semiconductor p−n Junction and Dominantly Exposed Reactive Facets. *Cryst. Growth Des.* **2016**, *16* (1), 221−228.

(38) Kern, R.; Sastrawan, R.; Ferber, J.; Stangl, R.; Luther, J. Modeling and interpretation of electrical impedance spectra of dye solar cells operated under open-circuit conditions. *Electrochim. Acta* **2002**, *47* (26), 4213−4225.

(39) Kresse, G.; Furthmüller, J. Efficiency of ab-initio total energy calculations for metals and semiconductors using a plane-wave basis set. *Comput. Mater. Sci.* **1996**, *6* (1), 15−50.

(40) Huang, H.; He, Y.; He, R.; Jiang, X.; Lin, Z.; Zhang, Y.; Wang, S. Novel Bi-Based Iodate Photocatalysts with High Photocatalytic Activity. *Inorg. Chem. Commun.* **2014**, *40*, 215−219.

(41) Lu, J.; Zeng, X.; Liu, H.; Zhang, W.; Zhang, Y. Preparation and Photoluminescence of (3C-ZnS)/(2H-ZnS) Superlattice in Mn-doped ZnS Nanoribbons. *J. Phys. Chem. C* **2012**, *116* (43), 23013−23018.

(42) Ma, X.; Wu, Y.; Lu, Y.; Xu, J.; Wang, Y.; Zhu, Y. Effect of Compensated Codoping on the Photoelectrochemical Properties of Anatase TiO_2 Photocatalyst. *J. Phys. Chem. C* **2011**, *115* (34), 16963−16969.

(43) Zhao, Z. Y.; Dai, W. W. Electronic Structure and Optical Properties of BiOI Ultrathin Films for Photocatalytic Water Splitting. *Inorg. Chem.* **2015**, *54* (22), 10732−7.